Energy &
Environmental
Science

PAPER

View Article Online
View Journal | View Issue

Cite this: *Energy Environ. Sci.*, 2017, **10**, 1476

Electrocatalysis of polysulfide conversion by sulfur-deficient MoS_2 nanoflakes for lithium–sulfur batteries†

Haibin Lin,[a] Liuqing Yang,[a] Xi Jiang,[a] Guochun Li,[a] Tianran Zhang,[a] Qiaofeng Yao,[a] Guangyuan Wesley Zheng*[ab] and Jim Yang Lee *[a]

Lithium–sulfur batteries are promising next-generation energy storage devices due to their high energy density and low material cost. Efficient conversion of lithium polysulfides to lithium sulfide (during discharge) and to sulfur (during recharge) is a performance-determining factor for lithium–sulfur batteries. Here we show that MoS_{2-x}/reduced graphene oxide (MoS_{2-x}/rGO) can be used to catalyze the polysulfide reactions to improve the battery performance. It was confirmed, through microstructural characterization of the materials, that sulfur deficiencies on the surface participated in the polysulfide reactions and significantly enhanced the polysulfide conversion kinetics. The fast conversion of soluble polysulfides decreased their accumulation in the sulfur cathode and their loss from the cathode by diffusion. Hence in the presence of a small amount of MoS_{2-x}/rGO (4 wt% of the cathode mass), high rate (8C) performance of the sulfur cathode was improved from a capacity of 161.1 mA h g^{-1} to 826.5 mA h g^{-1}. In addition, MoS_{2-x}/rGO also enhanced the cycle stability of the sulfur cathode from a capacity fade rate of 0.373% per cycle (over 150 cycles) to 0.083% per cycle (over 600 cycles) at a typical 0.5C rate. These results provide direct experimental evidence for the catalytic role of MoS_{2-x}/rGO in promoting the polysulfide conversion kinetics in the sulfur cathode.

Received 18th April 2017,
Accepted 15th May 2017

DOI: 10.1039/c7ee01047h

rsc.li/ees

Broader context

Among the alternatives proposed to succeed lithium-ion batteries, lithium–sulfur batteries have drawn the most interest because of the very high theoretical capacity of the sulfur cathode (about 1672 mA h g^{-1}). In addition, sulfur also has the benefits of being low cost, naturally abundant and environmentally benign. The development of lithium–sulfur batteries is however met with several technical challenges. The insulating properties of sulfur and its discharge products (Li_2S_2 and Li_2S) resulted in a slow discharge/charge process and a low practical capacity. The intermediate products formed during battery discharge and charge, *i.e.* lithium polysulfides (Li_2S_n, where $3 \leq n \leq 8$), are electrolyte soluble. The loss of sulfur electrochemically as dissolved lithium polysulfides is the cause of rapid capacity fading during cycling. This article reports the development of an electrocatalyst, MoS_{2-x}/reduced graphene oxide (MoS_{2-x}/rGO), which can accelerate the kinetics of polysulfide conversion reactions to insoluble products. Sulfur deficiencies in the MoS_2 nanoflakes were found to be the catalytic centers. The fast conversion of soluble polysulfides can lower their accumulation in the cathode, and hence their effusion from the electrode. Consequently lithium–sulfur batteries using this catalyst in the sulfur cathode could increase the battery rate performance and cycle stability.

Introduction

Among the next-generation rechargeable batteries proposed to succeed lithium-ion batteries, lithium–sulfur batteries have drawn the most interest because of the high theoretical capacity of the sulfur cathode (1672 mA h g^{-1}, about 10 times of that of a typical lithium-ion battery cathode).[1–4] Sulfur also has the advantages of low cost, natural abundance and environmental benignity. The development of lithium–sulfur batteries is however met with several technical challenges. The insulating properties of sulfur and its discharge products (Li_2S_2 and Li_2S) result in a slow discharge/charge process and a low practical capacity. The intermediate products formed during battery discharge and charge, *i.e.* lithium polysulfides (Li_2S_n, where $3 \leq n \leq 8$), are electrolyte soluble and as such can migrate to the lithium metal anode and deposit there.[5,6] The loss of electrochemically active lithium polysulfides leads to a rapid capacity fading during cycling.

---

[a] *Department of Chemical and Biomolecular Engineering, National University of Singapore, 10 Kent Ridge Crescent, Singapore 119260, Singapore. E-mail: cheleejy@nus.edu.sg*
[b] *Institute of Materials Research and Engineering (IMRE), A*STAR (Agency for Science, Technology and Research), 2 Fusionopolis Way, Innovis, #08-03, Singapore 138634. E-mail: wesley-zheng@imre.a-star.edu.sg*

† Electronic supplementary information (ESI) available. See DOI: 10.1039/c7ee01047h

The strategies developed to date to address these challenges consist mostly of the following: (i) new cathode designs to increase the electrode conductivity and polysulfide retention,[7–10] (ii) new electrolyte formulations,[11,12] separator structure[13–15] and binder chemistry[16,17] to minimize polysulfide migration, and (iii) surface engineering of the lithium metal anode to protect against passivation by the lithium polysulfides migrating from the cathode.[18–20] Although substantial progress has been made, these strategies are still far from realizing the full potential of the lithium–sulfur batteries.

Some recent research has considered the alternative of improving the kinetics of polysulfide conversion in the sulfur cathode.[21–23] During battery discharge and charge, the conversion between sulfur and its end products (Li_2S_2 and Li_2S) has to occur *via* lithium polysulfides as the intermediate products which are soluble in most lithium–sulfur battery electrolytes used today.[24] Since sulfur, Li_2S_2 and Li_2S are insoluble, accelerating the rates of conversion of soluble lithium polysulfides (to S, Li_2S_2 or Li_2S) can reduce the presence of polysulfides in the electrolyte, and hence their impact on the battery performance. This could improve both the sulfur utilization and the battery cycle stability. Although the use of polar compounds such as Magnéli phase Ti_4O_7 (2×10^3 S cm^{-1}),[23] metal-like TiC (10^4 S cm^{-1})[25] and CoS_2 (6.7×10^3 S cm^{-1})[22] as conductive sulfur hosts with good polarity for polysulfide adsorption has been known for some time, the use of platinum, nickel[21] and cobalt[26] as the "catalysts" for polysulfide conversion is a relatively recent development. As such the catalysis of polysulfide conversion is still in an early phase of research.

In the search for catalysts which can provide good performance at low cost, we discovered MoS_2 to be a strong candidate. MoS_2 has been shown to be highly effective for the catalysis of several industrially important reactions such as the hydrogen evolution reaction (HER), the oxygen reduction reaction (ORR) and the oxygen evolution reaction (OER).[27–30] MoS_2 with sulfur deficiencies, in particular, has drawn the most research interest because of the high electrochemical activity associated with the presence of sulfur deficiencies.[31,32] Indeed, our previous work on using MoS_2 as the lithium-ion battery anode has revealed some behavior of the lithium–sulfur batteries, but without the issues of low sulfur conductivity and polysulfide shuttle in discharge and charge.[33] Deficiencies such as MoS_2 edge sites and terrace surfaces have shown good electrochemical activity for Li_2S deposition.[34] Herein, rGO decorated with few-layer MoS_2 nanoflakes with a controlled amount of sulfur deficiency (MoS_{2-x}/rGO) was used to catalyze the polysulfide conversion in a sulfur cathode. The MoS_2 nanoflakes were prepared by the sonication assisted liquid phase exfoliation of commercial MoS_2 powder in *N*-methyl-2-pyrrolidone (NMP). The amount of sulfur deficiencies could be varied by changing the time and temperature in a heat treatment in hydrogen. The experimental results confirmed the involvement of surface sulfur deficiencies in the polysulfide conversion reactions and their catalytic effect on the kinetics of polysulfide conversion. In the presence of a small amount (4 wt% of the cathode mass) of MoS_{2-x}/rGO in the sulfur cathode, the sulfur cathode exhibited both high-rate capability (capacity of 826.5 mA h g^{-1} at an 8C rate) and good cycle stability (capacity fade rate of 0.083% per cycle for 600 cycles at a 0.5C rate). These performances place MoS_{2-x}/rGO as one of the best (if not the best) polysulfide conversion catalysts reported to date.

Experimental section

Chemicals

N-Methyl-2-pyrrolidone (NMP, 99.5 wt%), polyvinylidene fluoride (PVDF, 99.5 wt%), sulfur (99.5 wt%), lithium sulfide (Li_2S, 99.98 wt%), 1,3-dioxolane (DOL, 99.8 wt%), 1,2-dimethoxyethane (DME, 99.5 wt%), molybdenum(VI) oxide (MoO_3, 99.5%), lithium bis(trifluoromethanesulfonyl) imide (LiTFSI, 99.95 wt%) and lithium nitrate ($LiNO_3$, 99.99 wt%) from Sigma Aldrich; molybdenum(IV) sulfide (MoS_2, 99 wt%) from Alfa Aesar; and Super-P carbon (99.5 wt%) from Timcal were used as received.

Preparation of MoS_2 nanoflakes and MoS_2/GO composite

Few-layer MoS_2 nanoflakes were prepared by the sonication-assisted exfoliation of commercial MoS_2 powder in NMP.[35] In brief, 100 mg MoS_2 powder was dispersed in 20 mL NMP, and sonicated for 5 hours under ambient conditions. After centrifugation at 10 000 rpm for 5 minutes, the supernatant containing the MoS_2 nanoflakes was diluted with 30 mL water to form the MoS_2 stock solution. A graphene oxide (GO) sample prepared using a modified Hummer's method[36] was added to this solution and sonically homogenized for 10 minutes. The composite formed as such (MoS_2/GO) was recovered by vacuum filtration.

Preparation of MoS_{2-x}/rGO and MoS_2/rGO composites

MoS_2 nanoflakes with sulfur deficiencies (sulfur-deficient MoS_2 nanoflakes) were formed by heating the MoS_2/GO composite prepared above in a 10% H_2/Ar mixture. Different combinations of reaction temperature and time were used for the preparation. A MoS_2/rGO composite without the sulfur deficiencies was also prepared for performance comparison. Here the rGO was separately prepared by heating a GO sample in a 10% H_2/Ar atmosphere at 600 °C for 6 hours. The rGO was dispersed into the MoS_2 stock solution to a rGO/MoS_2 mass ratio of 8 : 2 (the same ratio as that of rGO to MoS_{2-x} in MoS_{2-x}/rGO), and sonically homogenized for 5 hours. The MoS_2/rGO composite was then recovered by vacuum filtration.

Preparation of rGO/S, MoS_2/rGO/S and MoS_{2-x}/rGO/S composites

rGO/S, MoS_2/rGO/S and MoS_{2-x}/rGO/S composites (the actual cathode materials for the lithium–sulfur test batteries) were prepared by the conventional melt-diffusion method. In brief sulfur powder and rGO (or MoS_{2-x}/rGO or MoS_2/rGO/S) in a 75 : 25 mass ratio were homogenized by grinding; and then sealed in a vial with Ar. The mixture was then heated at 155 °C for 5 hours to distribute the sulfur uniformly in rGO (or in MoS_2/rGO/S or MoS_{2-x}/rGO).

Materials characterization

The morphology of the composites in this study was examined by field emission scanning electron microscopy (FESEM) on a JEOL JSM-6700F SEM, by transmission electron microscopy (TEM) on a JEOL 2100F microscope, and by high-resolution TEM (HRTEM) on a JEOL 2100F system. The composite crystal structures were determined by X-ray diffraction (XRD) on a BRUKER D8 ADVANCE (Germany) instrument using Cu K_α radiation. X-ray photoelectron spectroscopy (XPS) analysis of the samples was performed on a Kratos AXIS Ultra DLD surface analyzer using a monochromatic Al K_α radiation source at 15 kV (1486.71 eV). The XPS peak locations were corrected by referencing the C 1s peak of adventitious carbon to 284.5 eV. Spectral deconvolution was carried out using the XPS Peak 4.1 software. The rGO and sulfur contents of the composites were analyzed by thermogravimetry (TGA) on a Shimadzu DTG-60H analyzer in air (for the measurement of the rGO content) or in N_2 (for the measurement of the sulfur content) at a temperature ramp rate of 10 °C min^{-1}.

Adsorption properties of lithium polysulfides

Li_2S and sulfur in amounts corresponding to the nominal stoichiometry of Li_2S_6 were added to a 1 : 1 (v/v) DOL/DME mixture and stirred overnight at 60 °C. The concentration of the Li_2S_6 solution prepared as such was 3 mmol L^{-1}, and was used as the stock solution for adsorption measurements. 10 mg rGO, MoS_2/rGO or MoS_{2-x}/rGO was added to 2 mL each of the lithium polysulfide stock solution. The mixtures were vigorously stirred to facilitate adsorption.

Cell assembly and electrochemical measurements

Symmetric electrochemical cells were assembled by the following procedure: 80 wt% active material (MoS_{2-x}/rGO, MoS_2/rGO, or rGO) and 20 wt% PVDF binder were homogenized in NMP to form a consistent slurry, which was then uniformly applied to an Al foil. The foil was cut into 1 cm × 1 cm sheets. The active material loadings on the sheets were about 2–4 mg. CR2025 coin cells were assembled in an Ar-filled M Braun glove box by using two coated Al sheets as the cathode and anode, a Celgard 2400 separator, and 50 μL electrolyte of 1 M LiTFSI and 0.2 M Li_2S_6 in a 1 : 1 (v/v) DOL/DME mixture. The counter electrode after the test was disassembled from the cell, rinsed with DOL thrice to remove the lithium salt on the surface; and then evacuated overnight at room temperature for *ex situ* analysis on the next day. Lithium–sulfur test batteries were assembled by a slightly different procedure: an NMP slurry of 80 wt% active material (MoS_{2-x}/rGO/S, MoS_2/rGO/S or rGO/S), 10 wt% Super P and 10 wt% PVDF was applied onto an Al foil to a loading of ~1.5 mg cm^{-2}. CR2025 coin cells were assembled using the coated Al foil as the cathode, a lithium metal foil anode, a Celgard 2400 separator, and 50 μL 1 M LiTFSI and 2 wt% $LiNO_3$ solution in DOL/DME (1 : 1 v/v) as the electrolyte. A Neware battery tester was used to regulate the cell discharge and charge. The cathode specific capacities were normalized only by the mass of sulfur, as per the common practice. Cyclic voltammetry (CV) and electrochemical impedance measurements were carried out on an Autolab type III electrochemical workstation.

Results and discussion

Fig. 1A shows the major steps in the preparation of MoS_{2-x}/rGO. The MoS_2 nanoflakes and GO (Fig. 1B) were co-dispersed in water; and then the mixed solid phase recovered by filtration was heated in a reducing hydrogen atmosphere at high temperature. The nanocomposite formed as such consisted of MoS_{2-x} nanoflakes on a thin film of rGO. rGO, a common substrate for electrochemical devices,[37–39] was used here as a flexible and conductive catalyst support. Fig. 1C is the TEM image of the MoS_2 nanoflakes formed by the liquid phase exfoliation of bulk commercial MoS_2 particles shown in Fig. S1 (ESI†). MoS_2 could be exfoliated into nanoflakes very easily by this procedure and formed a uniform dispersion in the solvent (Fig. S2, ESI†). The HRTEM image in Fig. 1D shows the layer-like structure of the MoS_2 nanoflakes, which were about 3–5 nm in thickness and consisted of 6–8 layers. The lattice spacing of 0.62 nm matches well with the (002) diffraction of hexagonal MoS_2.[40] The small MoS_2 nanoflakes were well dispersed on the rGO sheets. The high temperature treatment in hydrogen removed some sulfur atoms in the MoS_2 nanosheets to result in the formation of sulfur deficiencies. The geometric compatibility between the two 2D nanomaterials (rGO and MoS_2 nanosheets) should improve the quality of the interfacial contact, and the 2D-on-2D construction also allowed a good exposure of the sulfur deficiencies on the catalyst surface for the conversion of adsorbed polysulfides.

The effects of heat treatment temperature and time on the structure of the MoS_{2-x}/rGO composite were analyzed by XRD and XPS. The XRD patterns of samples prepared under different conditions are quite similar (Fig. 2A). The broad diffraction at around $2\theta = 20–30°$ can be attributed to the disorderly stacked rGO sheets. The diffraction peaks of the MoS_2 nanoflakes are in good agreement with the 2H phase of MoS_2 (PDF#37-1492),[41] and hence the phase purity of MoS_2 was good. The most intense MoS_2 peak was the (002) peak at $2\theta \sim 15°$, suggesting [001] as the crystal growth direction. Fig. 2B shows the expanded view of the MoS_2 (002) peak. There was a slight shift of this peak to lower 2θ values with the increase in treatment severity (higher temperature or longer heat treatment time). The shift indicates an increase in the lattice parameter[42] caused most likely by the removal of sulfur by hydrogen. The resultant reduction of Mo to a lower oxidation state with a larger atomic radius led to the increase in the lattice parameter.

The surface compositions of MoS_{2-x}/rGO composites prepared under different heat treatment conditions were characterized by XPS. The total molybdenum (Mo) and sulfur (S) contents of the samples as analyzed by XPS are summarized in Table S1 (ESI†). The Mo : S ratio of the as-synthesized MoS_2 nanoflakes was 33.2 : 65.4, close to the 1 : 2 ratio in stoichiometric MoS_2. The Mo : S ratio increased with the increase in reaction temperature and reaction time; indicating the progressive removal of the sulfur element. The Mo 3d spectra were deconvoluted to

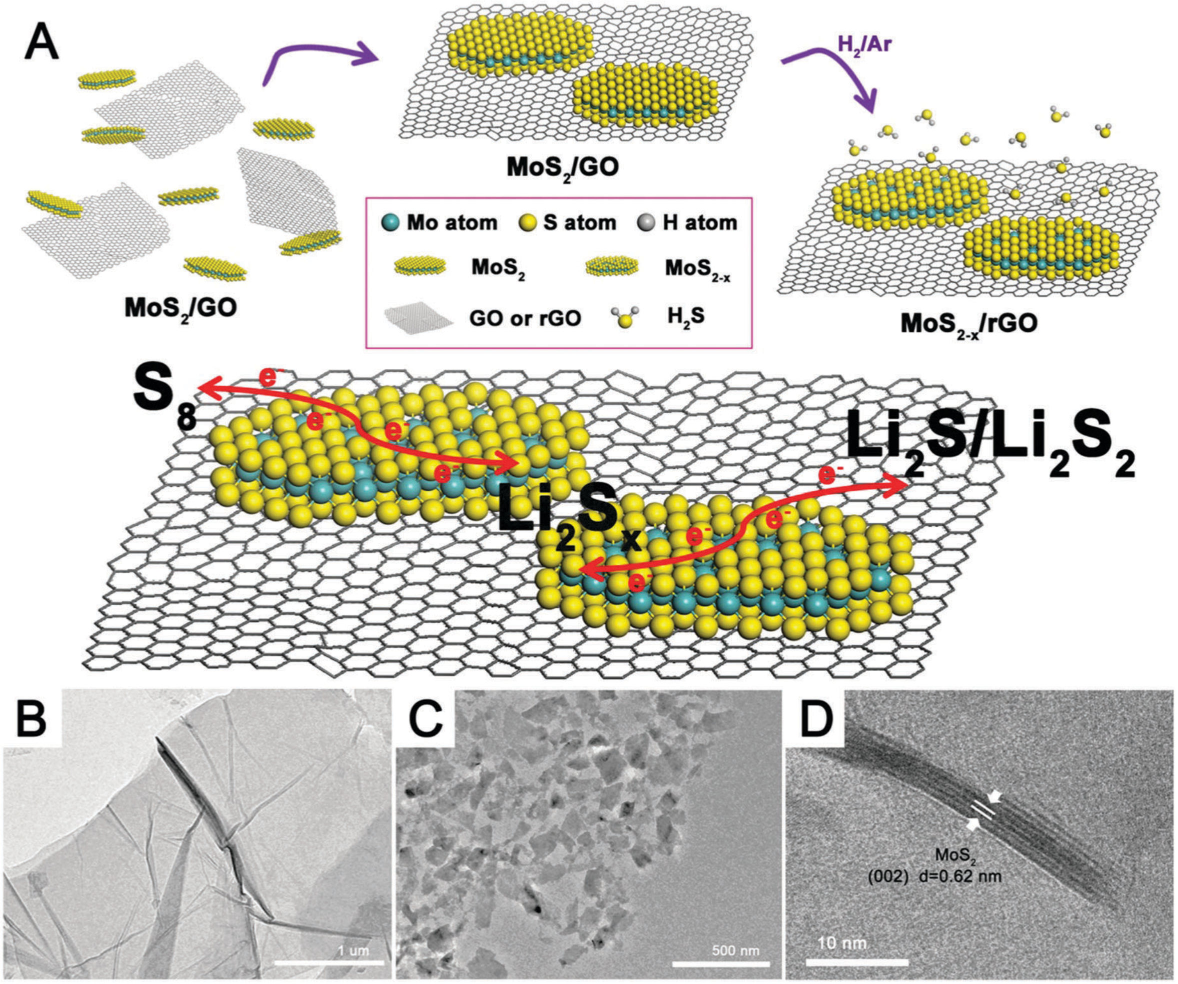

Fig. 1 (A) Schematic of the synthesis of the MoS_{2-x}/rGO composite and the conversion of Li_2S_x on the MoS_{2-x}/rGO surface. TEM images of (B) a thin GO film and (C) MoS_2 nanoflakes. (D) HRTEM image of MoS_2 nanoflakes.

determine the stoichiometric MoS_2 (red), the sulfur-deficient MoS_2 (blue) and the MoO_3 (green) contents of various samples (Fig. 2C).[43,44] Specifically the Mo $3d_{5/2}$ and $3d_{3/2}$ doublets at ~229.5 eV and 232.5 eV were deconvoluted into two sets of peaks. The first set of peaks with binding energies of 232.6 eV and 229.5 eV could be attributed to stoichiometric MoS_2, while the second set at lower binding energies (232.2 eV and 229.1 eV) could be assigned to sulfur-deficient MoS_2. The peak distinctively upstream of the MoS_2 peaks may be attributed to MoO_3 (green).[44] The appearance of MoO_3 could be attributed to the oxidation of some low oxidation state Mo atoms in MoS_2, as per the previous report.[35] The results showed that the increase in temperature and reaction time increased the amount of sulfur deficiency. The presence of MoO_3 in the 700 °C sample could be due to the oxidation of Mo metal clusters (which is highly susceptible to atmospheric oxidation). Thermal annealing of MoS_2 in a hydrogen environment could lead to the removal of sulfur atoms as H_2S gas and hence the formation of sulfur deficiencies. The excess Mo could also form Mo metal clusters.[59] The Mo metal clusters were oxidized to MoO_3 after the sample was removed from the heating chamber. MoO_3 could also be formed directly by the substitution of sulfur in MoS_2 with oxygen from GO during the heat treatment. Although the 700 °C sample contained a high sulfur deficiency content, the deep reduction of MoS_2 led to an unstable nanoflake structure (Fig. S3, ESI†) caused by the excessive expansion of the lattice parameter. The MoS_{2-x}/rGO composite with the highest sulfur deficiency content which could still preserve the nanoflake structure was prepared at 600 °C for 6 hours ($x = 0.42$).

The morphology of the stable high sulfur-deficiency MoS_{2-x}/rGO composite (prepared at 600 °C for 6 hours) was examined by both FESEM and TEM. The FESEM image in Fig. 3A shows that the composite mirrored the laminate structure of rGO synthesized under the same conditions (Fig. S4A, ESI†). TEM images (Fig. 3B and C) confirm the presence of MoS_{2-x} nanoflakes on the rGO sheets. The 0.62 nm lattice spacing in the HRTEM image of a MoS_{2-x} nanoflake sample (Fig. 3D) is the same as that of the (002) planes of hexagonal MoS_2 in Fig. 1D, indicating that the sulfur deficiencies did not alter the native MoS_2 structure. The rGO content in the MoS_{2-x}/rGO composite as calculated by TGA (Fig. S5, ESI†) was about 78 wt%. For comparison, a composite containing MoS_2 and rGO (reduced from GO by heating in

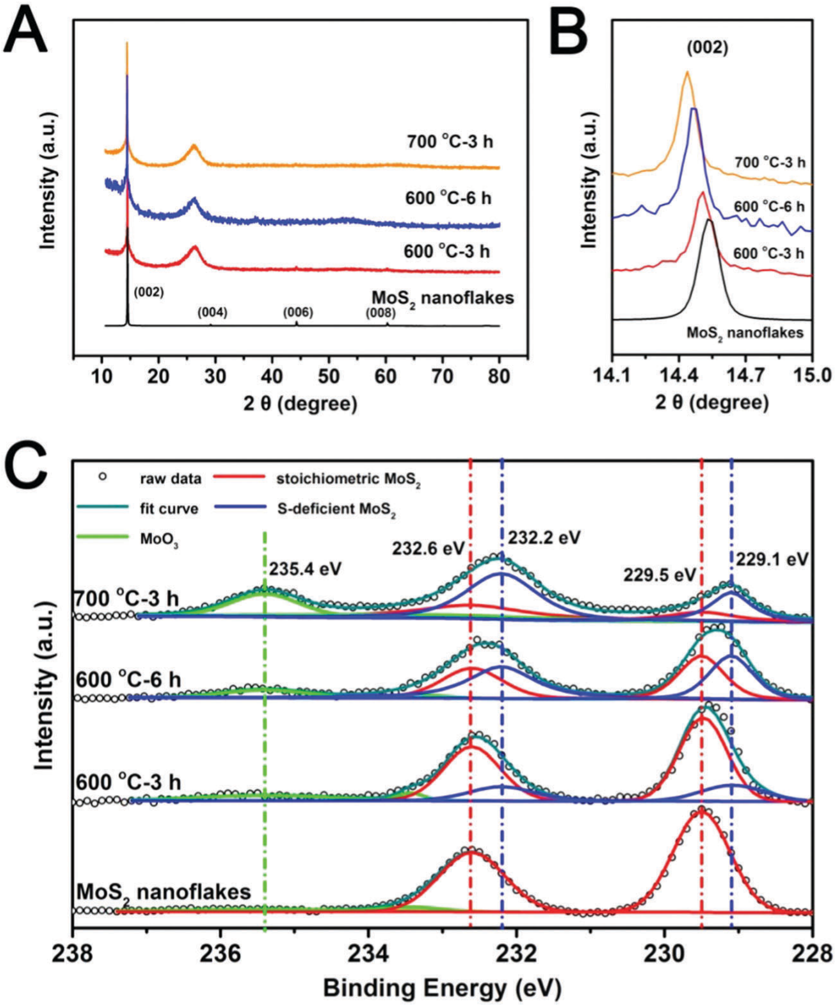

Fig. 2 (A and B) XRD patterns and (C) Mo 3d XPS spectra of MoS_2 nanoflakes and MoS_{2-x}/rGO composites formed by different combinations of reaction temperature and time in a hydrogen atmosphere.

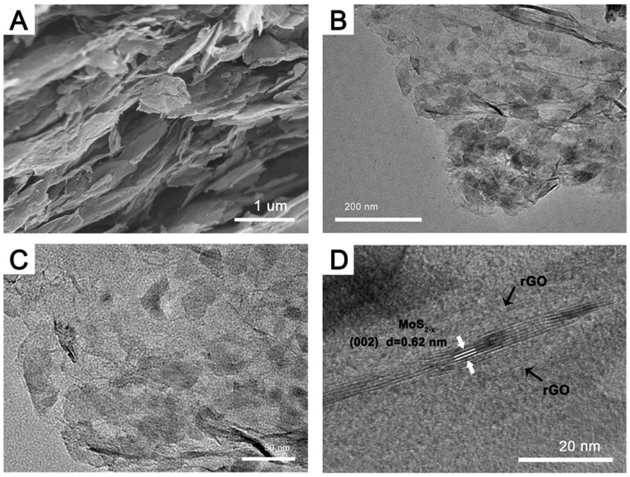

Fig. 3 (A) FESEM image, (B and C) TEM images and (D) HRTEM image of the MoS_{2-x}/rGO composite prepared by heating MoS_2/GO in a hydrogen atmosphere at 600 °C for 6 hours.

hydrogen at 600 °C for 6 hours), MoS_2/rGO, was also analyzed. The rGO content in the latter was similar, 77 wt%. TGA nonetheless detected higher thermal stability for rGO in MoS_{2-x}/rGO to suggest the stronger interaction between rGO and MoS_2 when the latter was sulfur deficient. Since sulfur deficiencies can render the MoS_{2-x} surface more electron rich,[45] and rGO formed below 600 °C has general p-type characteristics,[46] electron transfer from rGO to MoS_{2-x} may occur to develop a stronger bond between the two at their interface.[47] Such electron coupling is expected to contribute positively to the charge transfer at the MoS_{2-x}/rGO interface.

The catalytic effect of MoS_{2-x} on the polysulfide redox reactions was first revealed by CV in symmetric cells with identical working and counter electrodes in a 0.2 M Li_2S_6 electrolyte (Fig. 4A). MoS_2/rGO and rGO prepared under the same conditions were used as the experimental controls (Fig. 4B and C). The CV of a Li_2S_6-free electrolyte was also measured to correct for capacitive contributions. The voltammogram of the MoS_{2-x}/rGO electrode in the Li_2S_6 electrolyte exhibited high reversibility with four distinct peaks at −0.047 V, −0.39 V, 0.047 V and 0.39 V

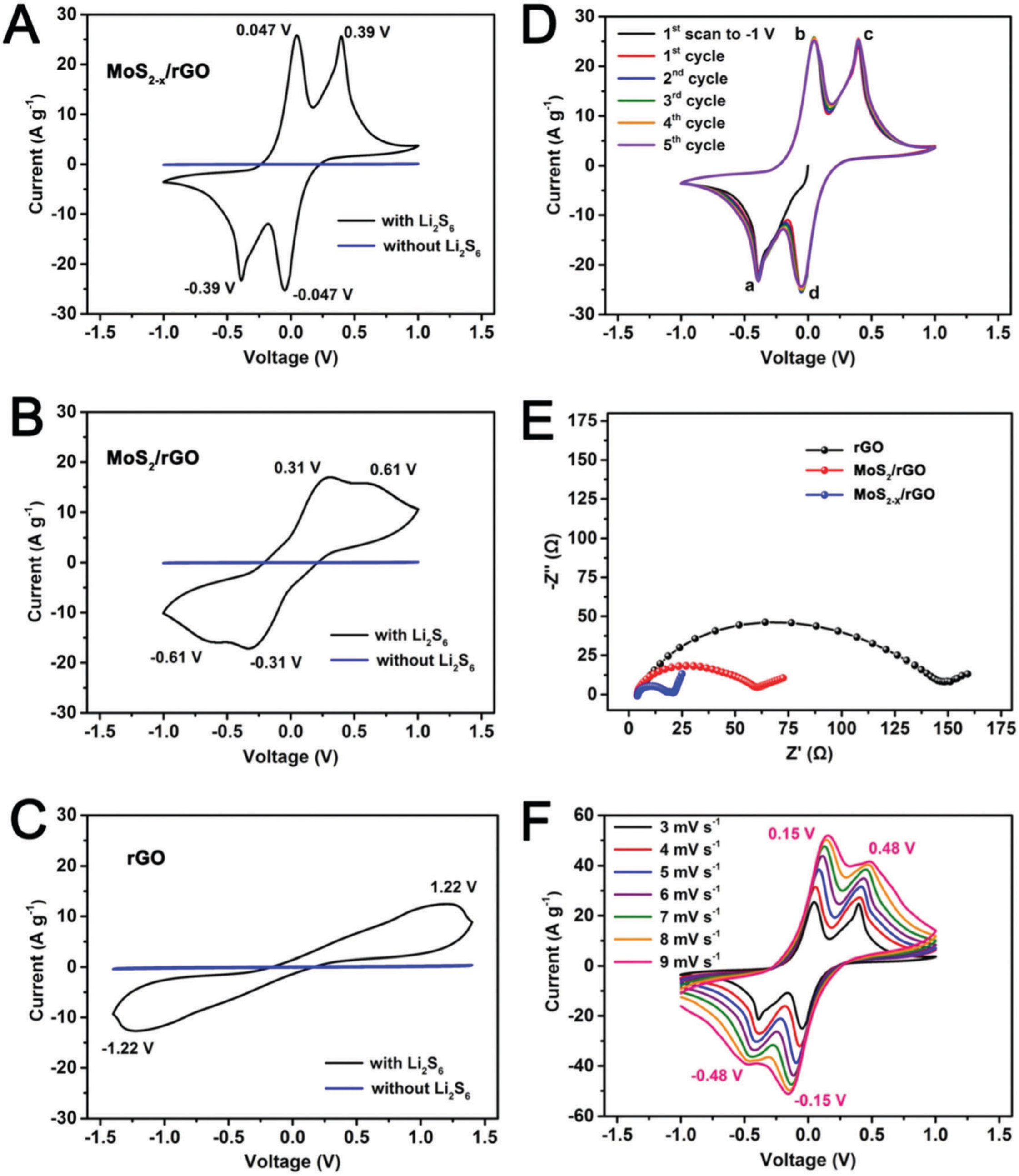

Fig. 4 Cyclic voltammograms of symmetric cells with identical electrodes of (A) MoS_{2-x}/rGO, (B) MoS_2/rGO and (C) rGO in electrolytes with and without 0.2 M Li_2S_6 at 3 mV s^{-1}. (D) Multi-cycle voltammograms of the MoS_{2-x}/rGO symmetric cell at 3 mV s^{-1}. (E) Electrochemical impedance spectra of the symmetric cells. (F) Voltammograms of the MoS_{2-x}/rGO symmetric cell at different scan rates.

respectively (Fig. 4A). The MoS_2/rGO electrode exhibited remnants of these peaks as broad redox features at −0.31 V, −0.61 V, 0.31 V and 0.61 V (Fig. 4B). For the rGO electrode, only a very drawn-out reduction peak at −1.22 V and a very drawn-out oxidation peak at 1.22 V were detected (Fig. 4C).

Fig. 4D shows the first five cycles of the MoS_{2-x}/rGO electrode in CV. The nearly perfect superimposition of the peaks suggests good stability of the sulfur-deficient MoS_{2-x}/rGO electrode. In the first cathodic scan from zero potential between the electrodes, only the peak at −0.39 V (peak a) appeared. The cathodic peak at −0.047 V (peak d) emerged only from the second scan onwards. Since Li_2S_6 was the only electrochemically active species in the electrolyte, it is reasonable to assume that Li_2S_6 was reduced to Li_2S (or Li_2S_2) on the working electrode, and oxidized to sulfur on the counter electrode in the cathodic scan. Hence the reduction of Li_2S_6 on the working electrode which manifested in peak a was complemented by the oxidation of Li_2S_6 on the counter electrode. Peak b in the following anodic scan was due to the reconstitution of Li_2S_6 by the oxidation of Li_2S (or Li_2S_2) on the working electrode. Similarly, peaks c and d identical in shape to peaks a and b were due to the oxidation of Li_2S_6 to sulfur, and the reduction of sulfur to

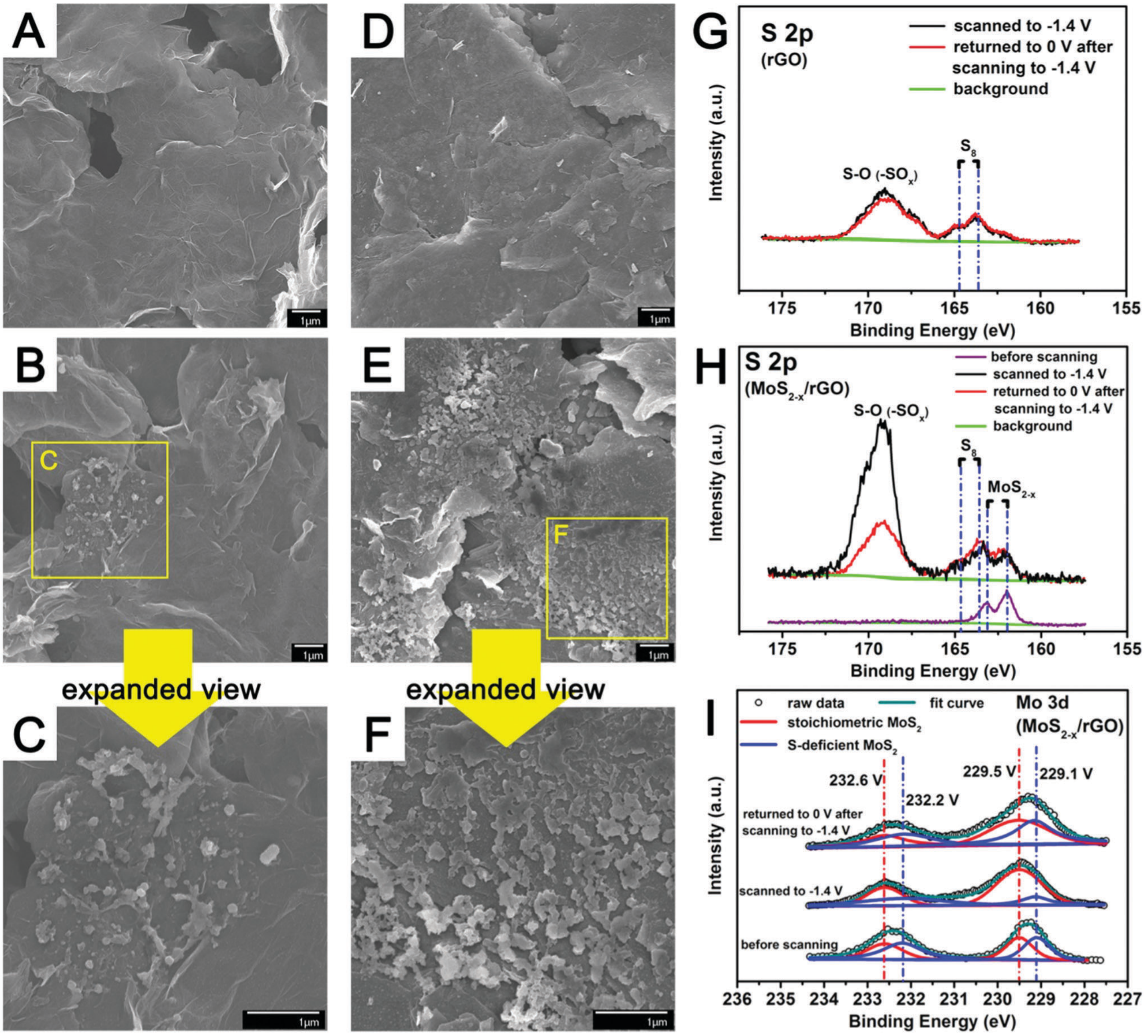

Fig. 5 FESEM images of (A) the pristine rGO electrode and (B and C) the rGO counter electrode removed from the symmetric cell after scanning to −1.4 V; (D) the pristine MoS_{2-x}/rGO electrode and (E and F) the MoS_{2-x}/rGO counter electrode after scanning to −1.4 V. XPS spectra of (G) the rGO and (H and I) MoS_{2-x}/rGO counter electrodes of symmetric cells after scanning to −1.4 V, or after scanning to −1.4 V and returning to 0 V.

Li_2S_6 on the working electrode respectively. Therefore, the peaks at −0.39 V/0.047 V and −0.047 V/0.39 V‡ were paired redox features of the symmetric cell. The reactions are summarized in Fig. S6 (ESI†). The sharpness of the peaks and the narrow peak separation in each redox pair indicate good electrochemical reversibility and facile polysulfide conversion. It should be mentioned that the two paired redox peaks related to the Li_2S_6 conversion reaction were absent in a previous study on CoS_2 using the symmetric cell.[22] The high scan rate (50 mV s^{-1}) and the narrow voltage range (from −0.7 V to 0.7 V) used in that study could have suppressed the detectability of these redox features. When the electrodes were MoS_2/rGO without the surface sulfur deficiencies, the broadened peaks and the increased peak separation are indications of reduced electrochemical reversibility and slower reactions (Fig. 4B).§ Electrochemical reversibility and conversion kinetics were the lowest with the rGO electrodes, resulting in the merging of peaks (Fig. 4C).

---

‡ These voltage values are potential differences between two redox reactions on two electrodes, and as such cannot be associated with half reactions.

§ We have also prepared another composite (MoS_{2-x}/rGO-2) by mixing rGO and MoS_{2-x} in water, and used it as the electrodes of a symmetric cell (Fig. S7, ESI†). Its redox performance was slightly inferior to the MoS_{2-x}/rGO electrode due to the poor mixing between MoS_{2-x} and rGO by this preparation route, which increased the likelihood of nanoflake aggregation. Nonetheless, sharper and narrower redox peaks were still obtained relative to the MoS_2/rGO electrode. The positive effect of sulfur deficiencies on polysulfide conversion was again demonstrated.

The polarity-induced adsorption between the polysulfides and a polar sulfide surface may have contributed to the more facile kinetics of polysulfide conversion on MoS_2/rGO and MoS_{2-x}/rGO (the apolar rGO surface is antagonistic to polysulfide adsorption).[48] This was demonstrated by a simple visual adsorption test (Fig. S8, ESI†) where the adsorption of Li_2S_6 on MoS_2/rGO and MoS_{2-x}/rGO completely decolorized the polysulfide solution. Electrochemical impedance spectroscopy (Fig. 4E) also registered the smallest charge transfer resistance (the size of the high frequency semicircle in the Nyquist plot) for the MoS_{2-x}/rGO symmetric cell. In the CVs measured at different scan rates (Fig. 4F), there were some slight shifts of the redox peaks with the increase in the scan rate. However, the peak separation in the MoS_{2-x}/rGO cell at a high scan rate of 9 mV s^{-1} was still significantly narrower than the peak separations in the MoS_2/rGO or rGO cells at 3 mV s^{-1}. All the above are evidence for the greatly enhanced kinetics of polysulfide conversion on the MoS_{2-x}/rGO surface.

For additional insights into the reactions of polysulfides on the MoS_{2-x}/rGO surface, the counter electrodes of symmetric cells with MoS_{2-x}/rGO or rGO electrodes after scanning from 0 V to −1.4 V were examined by FESEM.¶ Fig. 5 shows the FESEM images of the rGO (A–C) and the MoS_{2-x}/rGO (D–F) counter electrodes before and after scanning to −1.4 V. The larger number of sulfur particles and their more uniform distribution on the MoS_{2-x}/rGO surface could only come from the presence of more electrochemically active sites for polysulfide conversion. XPS was also used to analyze the surfaces of the counter electrodes of symmetric cells after scanning from 0 to −0.14 V, and from −0.14 V to 0 V. Fig. 5G and H show, respectively, the S 2p XPS spectra of the rGO and MoS_{2-x}/rGO counter electrodes. The 163.5 eV and 164.7 eV peaks could be attributed to the sulfur deposited on the counter electrodes, while the very prominent peak at ∼169 eV to the S–O bond in oxidized sulfur species such as $-SO_x$.[21] Since sulfur deposition on the counter electrode was mostly completed when the symmetric cells were scanned to −0.39 V (Fig. 4D), the sulfur deposit would be extensively oxidized when the cells were scanned to −1.4 V. The stronger S–O peak from the MoS_{2-x}/rGO cell can then be used as an indirect evidence for more sulfur formation in this cell (Fig. 5G and H). When this symmetric cell was returned to 0 V from −1.4 V, the decrease in the S–O peak intensity was caused by the electrochemical reduction of the oxidized sulfur species on the counter electrode. In contrast, the S–O peak from the rGO symmetric cell underwent very minor intensity changes from −1.4 V to 0 V, an indication of the limited sulfur presence on the rGO surface. The more extensive sulfur formation and reduction reactions in the MoS_{2-x}/rGO cell could only be caused by the existence of catalytically more active sites on the MoS_{2-x}/rGO surface. There was also evidence in the Mo 3d XPS spectra for the interaction between MoS_{2-x} and polysulfides during the polysulfide conversion reactions (Fig. 5I). When the symmetric cells were scanned to −1.4 V, the sulfur-deficient MoS_2 component (blue curve) in MoS_{2-x}/rGO was significantly diminished in intensity. It is believed that the deficiencies in MoS_{2-x} rendered the surface of MoS_{2-x}/rGO electron-rich. The XPS results of Fig. 5I indicate a weaker XPS signal from the sulfur deficiencies after sulfur deposition, suggesting the electron transfer from the former to the latter.[43,49,50] It has been reported in the oxygen reduction reaction (ORR) research that oxygen adsorption on an oxygen-deficient surface would elongate the O–O bond for an easier reduction.[56] The sulfur deficiencies on the MoS_{2-x}/rGO surface may likewise facilitate the reduction of sulfur to polysulfides, probably through the involvement of some metastable $S_x^{\bullet -}$ species.[57,58] When the symmetric cell was scanned back to 0 V, XPS showed that the sulfur deficiencies were restored, and hence the reversibility of the overall process. These changes establish the correspondence between sulfur deficiency and the extent and reversibility of polysulfide conversion, and provide indirect proof for sulfur deficiencies as the origin of enhanced catalytic activity in polysulfide electrochemical reactions.

The actual performance of MoS_{2-x}/rGO as a catalyst in lithium–sulfur batteries was evaluated in coin cells using a MoS_{2-x}/rGO/S composite cathode and a lithium metal anode. Coin cells with a MoS_2/rGO/S or rGO/S cathode were also assembled for comparison. The sulfur contents in the composites as assayed by TGA were about 75 wt% (Fig. S9, ESI†). Fig. 6A shows the typical voltammograms and the galvanostatic discharge–charge voltage profile of the MoS_{2-x}/rGO/S cathodes between 1.8 and 2.6 V. Since lithiation of MoS_2 occurs below 1.5 V *vs.* Li/Li^+, the MoS_2 nanoflakes would not have contributed to any capacity in the 1.8–2.6 V voltage range.[51] The two cathodic peaks at about 2.3 V and 2.0 V could be associated with the reduction of sulfur to soluble long-chain lithium polysulfides (Li_2S_x, $4 \le x \le 8$), and the subsequent conversion of the latter to insoluble short-chain polysulfides (Li_2S_2/Li_2S) respectively. The two peaks in the reverse anodic scan at about 2.3 V and 2.4 V represent the reverse reactions of the conversion of short-chain polysulfides to sulfur.[52,53] The two distinct discharge voltage plateaus (at ∼2.34 V and 2.12 V) at the 0.5C rate could be attributed to the conversion of sulfur to long-chain lithium polysulfides, and the formation of Li_2S_2/Li_2S from the latter. The reverse of these reactions occurred during charge to form two corresponding voltage plateaus at ∼2.23 V and 2.35 V respectively. The galvanostatic discharge and charge curves are therefore in agreement with the voltammograms.[54,55] The generally intense peaks on MoS_{2-x}/rGO/S indicate the great extent of the polysulfide conversion due to the fast electrode kinetics.

Fig. 6B compares the electrochemical performance of the MoS_{2-x}/rGO/S, MoS_2/rGO/S and rGO/S cathodes at different C-rates (from 0.2C to 8C; 1C = 1600 mA g^{-1}). The first cycle discharge capacities of rGO/S, MoS_2/rGO/S and MoS_{2-x}/rGO/S at the 0.2C rate were 1210.5 mA h g^{-1}, 1243.2 mA h g^{-1} and 1310.5 mA h g^{-1} respectively. The capacity difference deviated more at higher rates, and was 826.5 mA h g^{-1} for MoS_{2-x}/rGO/S (63.1% of its 0.2C capacity), 473.3 mA h g^{-1} for MoS_2/rGO/S (38.1% of its 0.2C capacity) and 161.1 mA h g^{-1} for rGO/S (13.3% of its 0.2C capacity) at the 8C rate, which was the test

---

¶ The counter electrode instead of the working electrode was analysed because it was where sulfur was deposited. The Li_2S or Li_2S_2 on the working electrode is prone to decomposition by atmospheric moisture, which could increase the difficulty in result interpretation.

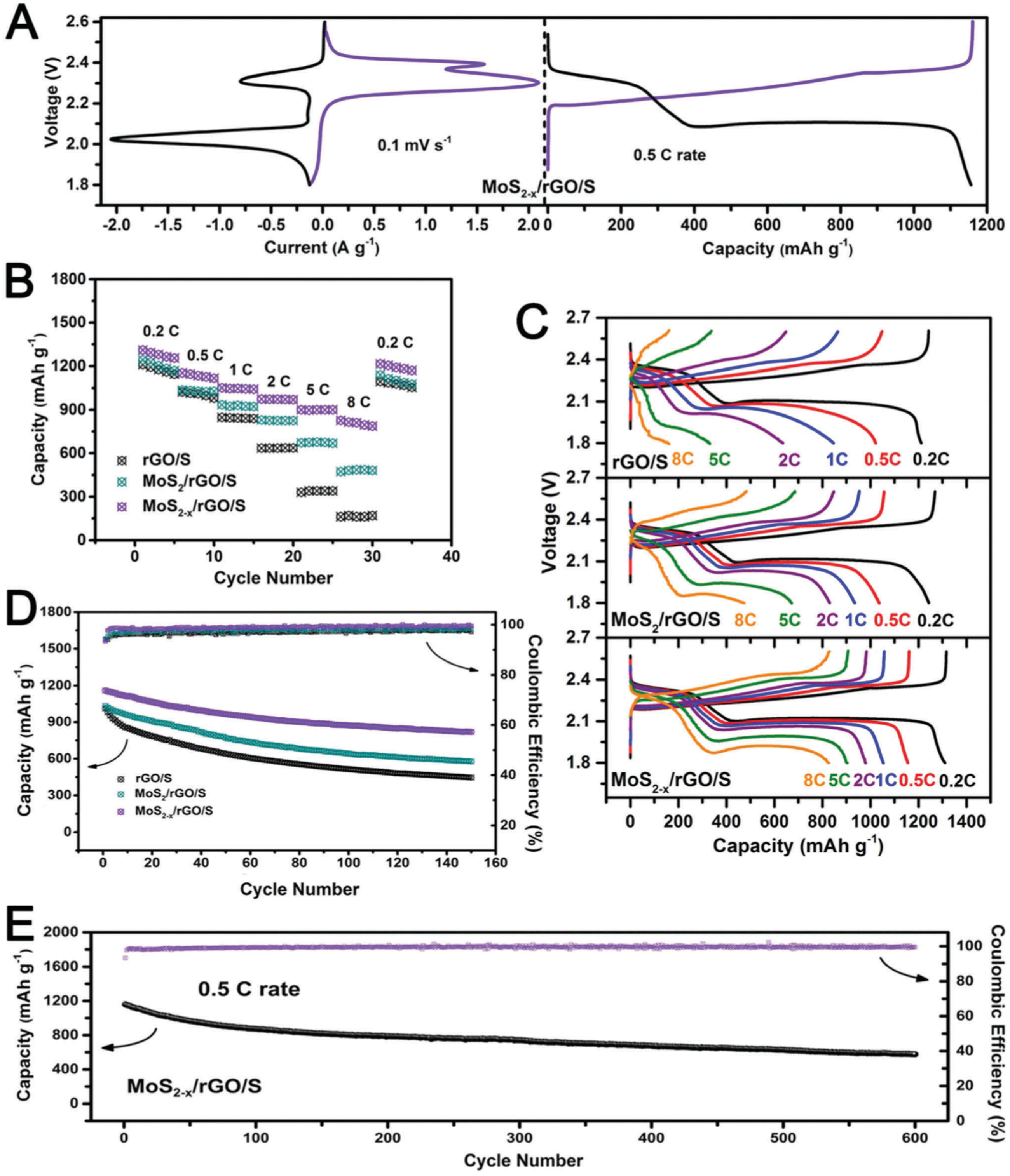

Fig. 6 (A) Cyclic voltammograms at 0.1 mV s^{-1} and the representative galvanostatic discharge–charge voltage profile at 0.5C, (B) comparison of rate performance at different C-rates, (C) galvanostatic discharge–charge curves and (D and E) cycle stability of rGO/S, MoS_2/rGO/S and MoS_{2-x}/rGO/S cells in the 1.8–2.6 V voltage range at 0.5C (1C = 1600 mA g^{-1} based on the mass of sulfur).

limit of this study. The higher affinity of MoS_{2-x}/rGO for polysulfide adsorption and the catalytic effect of sulfur deficiencies in MoS_2 for polysulfide conversion are expected to be the contributive factors although their respective contributions are difficult to resolve at this time. Fig. 6C shows the galvanostatic discharge and charge curves of the cells at different C-rates. An increase in the C-rate caused the charge voltage plateaus to shift positively and the discharge voltage plateaus to shift negatively. The voltage plateaus at the 8C rate were clearly visible in the MoS_{2-x}/rGO/S cell, due to the more facile electrode kinetics on MoS_{2-x}/rGO.

The cyclabilities of the MoS_{2-x}/rGO/S, MoS_2/rGO/S and rGO/S cathodes at the typical 0.5C rate are compared in Fig. 6D. Not only were the rGO/S and MoS_2/rGO/S cathodes lower in initial capacity (1013.3 mA h g^{-1} and 1033 mA h g^{-1}), they also exhibited more severe capacity fading endings with 445.3 mA h g^{-1} and 576.4 mA h g^{-1} after 150 cycles. In contrast, the MoS_{2-x}/rGO/S cathode exhibited both higher discharge capacity and greater cycle stability (initial discharge capacity of 1159.9 mA h g^{-1} and capacity of 819.9 mA h g^{-1} after 150 cycles). The long-term cycling performance of MoS_{2-x}/rGO/S at the 0.5C rate was also evaluated (Fig. 6E). After 600 cycles of continuous cycling, a discharge capacity of 628.2 mA h g^{-1} remained (a capacity fade rate of 0.083% per cycle). The Coulombic efficiency was as high as 99.6%. Cycle stability was thereof another benefit of the catalysis of polysulfide conversion in the sulfur electrode. A higher conversion rate of soluble polysulfides to insoluble sulfur products could decrease their accumulation in the cathode and consequently, their loss from the cathode by diffusion. Greater cycle stability was therefore realized by suppressing a major capacity loss mechanism. Compared to other catalysts in use today for the lithium–sulfur batteries (Table S2, ESI†), MoS_{2-x}/rGO is clearly a well-rounded choice with a strong performance in almost all functional categories.

Conclusions

In this study, we demonstrated the effectiveness of MoS_{2-x}/rGO as a catalyst for polysulfide conversion in a sulfur cathode. It was confirmed that the surface sulfur deficiencies participated in the polysulfide conversion and catalyzed the kinetics of polysulfide redox reactions. When a small amount of MoS_{2-x}/rGO (4 wt%) was added to the sulfur cathode, high-rate performance and good cycle stability of the batteries were obtained. The high rate performance could be attributed to the acceleration of the polysulfide conversion kinetics on the surface sulfur deficiencies. The fast conversion of soluble polysulfides decreased their accumulation in the sulfur cathode and inhibited their subsequent loss from the cathode by diffusion. The suppression of this loss mechanism led to a more sustained cyclability. The study here not only presented a catalyst candidate which is among the best reported to date, but it also provided experimental evidence for and some new insights into the origin of the catalytic effects.

Acknowledgements

H. L. acknowledges the National University of Singapore for his research scholarship.

References

1 W. Zhou, B. Guo, H. Gao and J. B. Goodenough, *Adv. Energy Mater.*, 2016, **6**, 1502059.

2 J. Li, L. Yang, S. Yang and J. Y. Lee, *Adv. Energy Mater.*, 2015, **5**, 1501808.

3 J. Zhang, H. Hu, Z. Li and X. W. Lou, *Angew. Chem., Int. Ed.*, 2016, **55**, 3982–3986.

4 M. Wild, L. O'Neill, T. Zhang, R. Purkayastha, G. Minton, M. Marinescu and G. J. Offer, *Energy Environ. Sci.*, 2015, **8**, 3477–3494.

5 Y. X. Yin, S. Xin, Y. G. Guo and L. J. Wan, *Angew. Chem., Int. Ed.*, 2013, **52**, 13186–13200.

6 Q. Pang, X. Liang, C. Y. Kwok and L. F. Nazar, *Nat. Energy*, 2016, **1**, 16132.

7 X. Ji, K. T. Lee and L. F. Nazar, *Nat. Mater.*, 2009, **8**, 500–506.

8 H.-J. Peng, J.-Q. Huang, M.-Q. Zhao, Q. Zhang, X.-B. Cheng, X.-Y. Liu, W.-Z. Qian and F. Wei, *Adv. Funct. Mater.*, 2014, **24**, 2772–2781.

9 G. Zheng, Q. Zhang, J. J. Cha, Y. Yang, W. Li, Z. W. Seh and Y. Cui, *Nano Lett.*, 2013, **13**, 1265–1270.

10 X. Wang, T. Gao, X. Fan, F. Han, Y. Wu, Z. Zhang, J. Li and C. Wang, *Adv. Funct. Mater.*, 2016, **26**, 7164–7169.

11 S. Zhang, K. Ueno, K. Dokko and M. Watanabe, *Adv. Energy Mater.*, 2015, **5**, 1500117.

12 J. Chen, K. S. Han, W. A. Henderson, K. C. Lau, M. Vijayakumar, T. Dzwiniel, H. Pan, L. A. Curtiss, J. Xiao, K. T. Mueller, Y. Shao and J. Liu, *Adv. Energy Mater.*, 2016, **6**, 1600160.

13 J. Balach, T. Jaumann, M. Klose, S. Oswald, J. Eckert and L. Giebeler, *Adv. Funct. Mater.*, 2015, **25**, 5285–5291.

14 S. H. Chung and A. Manthiram, *Adv. Mater.*, 2014, **26**, 1360–1365.

15 J.-Q. Huang, Q. Zhang, H.-J. Peng, X.-Y. Liu, W.-Z. Qian and F. Wei, *Energy Environ. Sci.*, 2014, **7**, 347–353.

16 P. Bhattacharya, M. I. Nandasiri, D. Lv, A. M. Schwarz, J. T. Darsell, W. A. Henderson, D. A. Tomalia, J. Liu, J.-G. Zhang and J. Xiao, *Nano Energy*, 2016, **19**, 176–186.

17 T. Nakazawa, A. Ikoma, R. Kido, K. Ueno, K. Dokko and M. Watanabe, *J. Power Sources*, 2016, **307**, 746–752.

18 G. Zheng, S. W. Lee, Z. Liang, H. W. Lee, K. Yan, H. Yao, H. Wang, W. Li, S. Chu and Y. Cui, *Nat. Nanotechnol.*, 2014, **9**, 618–623.

19 W. Xu, J. Wang, F. Ding, X. Chen, E. Nasybulin, Y. Zhang and J.-G. Zhang, *Energy Environ. Sci.*, 2014, **7**, 513–537.

20 Y. Yang, G. Zheng and Y. Cui, *Energy Environ. Sci.*, 2013, **6**, 1552.

21 H. Al Salem, G. Babu, C. V. Rao and L. M. Arava, *J. Am. Chem. Soc.*, 2015, **137**, 11542–11545.

22 Z. Yuan, H. J. Peng, T. Z. Hou, J. Q. Huang, C. M. Chen, D. W. Wang, X. B. Cheng, F. Wei and Q. Zhang, *Nano Lett.*, 2016, **16**, 519–527.

23 Q. Pang, D. Kundu, M. Cuisinier and L. F. Nazar, *Nat. Commun.*, 2014, **5**, 4759.

24 Y. Gorlin, M. U. M. Patel, A. Freiberg, Q. He, M. Piana, M. Tromp and H. A. Gasteiger, *J. Electrochem. Soc.*, 2016, **163**, A930–A939.

25 H. J. Peng, G. Zhang, X. Chen, Z. W. Zhang, W. T. Xu, J. Q. Huang and Q. Zhang, *Angew. Chem., Int. Ed.*, 2016, **55**, 12990–12995.

26 Y.-J. Li, J.-M. Fan, M.-S. Zheng and Q.-F. Dong, *Energy Environ. Sci.*, 2016, **9**, 1998–2004.

27 K. Chang, Z. Mei, T. Wang, Q. Kang, S. Ouyang and J. Ye, *ACS Nano*, 2014, **8**, 7078–7087.

28 J. Kibsgaard, Z. Chen, B. N. Reinecke and T. F. Jaramillo, *Nat. Mater.*, 2012, **11**, 963–969.

29 D. Kiriya, P. Lobaccaro, H. Y. Nyein, P. Taheri, M. Hettick, H. Shiraki, C. M. Sutter-Fella, P. Zhao, W. Gao, R. Maboudian, J. W. Ager and A. Javey, *Nano Lett.*, 2016, **16**, 4047–4053.

30 M. Asadi, B. Kumar, C. Liu, P. Phillips, P. Yasaei, A. Behranginia, P. Zapol, R. F. Klie, L. A. Curtiss and A. Salehi-Khojin, *ACS Nano*, 2016, **10**, 2167–2175.

31 Y. Yin, J. Han, Y. Zhang, X. Zhang, P. Xu, Q. Yuan, L. Samad, X. Wang, Y. Wang, Z. Zhang, P. Zhang, X. Cao, B. Song and S. Jin, *J. Am. Chem. Soc.*, 2016, **138**, 7965–7972.

32 H. Li, C. Tsai, A. L. Koh, L. Cai, A. W. Contryman, A. H. Fragapane, J. Zhao, H. S. Han, H. C. Manoharan, F. Abild-Pedersen, J. K. Norskov and X. Zheng, *Nat. Mater.*, 2016, **15**, 48–53.

33 G. Ji, Y. Yu, Q. Yao, B. Qu, D. Chen, W. Chen, J. Xie and J. Y. Lee, *NPG Asia Mater.*, 2016, **8**, e247.

34 H. Wang, Q. Zhang, H. Yao, Z. Liang, H.-W. Lee, P.-C. Hsu, G. Zheng and Y. Cui, *Nano Lett.*, 2014, **14**, 7138–7144.

35 A. Jawaid, D. Nepal, K. Park, M. Jespersen, A. Qualley, P. Mirau, L. F. Drummy and R. A. Vaia, *Chem. Mater.*, 2016, **28**, 337–348.

36 W. Tang, B.-M. Goh, M. Y. Hu, C. Wan, B. Tian, X. Deng, C. Peng, M. Lin, J. Z. Hu and K. P. Loh, *J. Phys. Chem. C*, 2016, **120**, 2600–2608.

37 B. Qu, C. Ma, G. Ji, C. Xu, J. Xu, Y. S. Meng, T. Wang and J. Y. Lee, *Adv. Mater.*, 2014, **26**, 3854–3859.

38 J. Wu, M. Liu, P. P. Sharma, R. M. Yadav, L. Ma, Y. Yang, X. Zou, X. D. Zhou, R. Vajtai, B. I. Yakobson, J. Lou and P. M. Ajayan, *Nano Lett.*, 2016, **16**, 466–470.

39 F. Wu, J. Li, Y. Su, J. Wang, W. Yang, N. Li, L. Chen, S. Chen, R. Chen and L. Bao, *Nano Lett.*, 2016, **16**, 5488–5494.

40 M. Thripuranthaka, R. V. Kashid, C. Sekhar Rout and D. J. Late, *Appl. Phys. Lett.*, 2014, **104**, 081911.

41 X. Fan, P. Xu, Y. C. Li, D. Zhou, Y. Sun, M. A. Nguyen, M. Terrones and T. E. Mallouk, *J. Am. Chem. Soc.*, 2016, **138**, 5143–5149.

42 J. Xiao, X. Chen, P. V. Sushko, M. L. Sushko, L. Kovarik, J. Feng, Z. Deng, J. Zheng, G. L. Graff, Z. Nie, D. Choi, J. Liu, J.-G. Zhang and M. S. Whittingham, *Adv. Mater.*, 2012, **24**, 2109–2116.

43 D. M. Sim, M. Kim, S. Yim, M.-J. Choi, J. Choi, S. Yoo and Y. S. Jung, *ACS Nano*, 2015, **9**, 12115–12123.

44 I. S. Kim, V. K. Sangwan, D. Jariwala, J. D. Wood, S. Park, K.-S. Chen, F. Shi, F. Ruiz-Zepeda, A. Ponce, M. Jose-Yacaman, V. P. Dravid, T. J. Marks, M. C. Hersam and L. J. Lauhon, *ACS Nano*, 2014, **8**, 10551–10558.

45 L.-p. Feng, J. Su and Z.-t. Liu, *RSC Adv.*, 2015, **5**, 20538–20544.

46 N. D. K. Tu, J. Choi, C. R. Park and H. Kim, *Chem. Mater.*, 2015, **27**, 7362–7369.

47 X. Wang, G. Li, M. H. Seo, F. M. Hassan, M. A. Hoque and Z. Chen, *Adv. Energy Mater.*, 2015, **5**, 1501106.

48 Q. Pang and L. F. Nazar, *ACS Nano*, 2016, **10**, 4111–4118.

49 H.-J. Peng, Z.-W. Zhang, J.-Q. Huang, G. Zhang, J. Xie, W.-T. Xu, J.-L. Shi, X. Chen, X.-B. Cheng and Q. Zhang, *Adv. Mater.*, 2016, **28**, 9551–9558.

50 E. Gracia-Espino, G. Hu, A. Shchukarev and T. Wågberg, *J. Am. Chem. Soc.*, 2014, **136**, 6626–6633.

51 J. Ye, W. Chen, Q. Chen, Z. Yu and J. Y. Lee, *Electrochim. Acta*, 2016, **190**, 538–547.

52 L. Wang, Y. Wang and Y. Xia, *Energy Environ. Sci.*, 2015, **8**, 1551–1558.

53 C. Wang, X. Wang, Y. Yang, A. Kushima, J. Chen, Y. Huang and J. Li, *Nano Lett.*, 2015, **15**, 1796–1802.

54 K. Park, J. H. Cho, J.-H. Jang, B.-C. Yu, A. T. De La Hoz, K. M. Miller, C. J. Ellison and J. B. Goodenough, *Energy Environ. Sci.*, 2015, **8**, 2389–2395.

55 J. Liu, W. Li, L. Duan, X. Li, L. Ji, Z. Geng, K. Huang, L. Lu, L. Zhou, Z. Liu, W. Chen, L. Liu, S. Feng and Y. Zhang, *Nano Lett.*, 2015, **15**, 5137–5142.

56 F. Cheng, T. Zhang, Y. Zhang, J. Du, X. Han and J. Chen, *Angew. Chem., Int. Ed.*, 2013, **52**, 2474–2477.

57 H. L. Wu, L. A. Huff and A. A. Gewirth, *ACS Appl. Mater. Interfaces*, 2015, **7**, 1709–1719.

58 D.-H. Han, B.-S. Kim, S.-J. Choi, Y. Jung, J. Kwak and S.-M. Park, *J. Electrochem. Soc.*, 2004, **151**, E283.

59 D. Kiriya, P. Lobaccaro, H. Y. Y. Nyein, P. Taheri, M. Hettick, H. Shiraki, C. M. Sutter-Fella, P. Zhao, W. Gao, R. Maboudian, J. W. Ager and A. Javey, *Nano Lett.*, 2016, **16**, 4047–4053.